Exploiting radiative cooling for uninterrupted 24-hour water harvesting from the atmosphere

Journal Article

Author(s):
Haechler, Iwan; Park, Hyunchul; Schnoering, Gabriel; Gulich, Tobias; Rohner, Mathieu; Tripathy, Abinash; Milionis, Athanasios; Schutzius, Thomas Michael; Poulikakos, Dimos

Publication date:
2021

Permanent link:
https://doi.org/https://doi.org/10.3929/ethz-b-000491112

Originally published in:
Science Advances 7(26), https://doi.org/10.1126/sciadv.abf3978

Funding acknowledgement:
- On the fundamental role of substrate compliance and enhanced light absorption on droplet condensation and evaporation ()
- HierARchical Multiscale NanoInterfaces for enhanced Condensation processes ()

Science Advances
AAAS

advances.sciencemag.org/cgi/content/full/7/26/eabf3978/DC1

Supplementary Materials for

Exploiting radiative cooling for uninterrupted 24-hour water harvesting from the atmosphere

Iwan Haechler, Hyunchul Park, Gabriel Schnoering, Tobias Gulich, Mathieu Rohner, Abinash Tripathy, Athanasios Milionis, Thomas M. Schutzius*, Dimos Poulikakos*

*Corresponding author. Email: dpoulikakos@ethz.ch (D.P.); thomschu@ethz.ch (T.M.S.)

Published 23 June 2021, *Sci. Adv.* **7**, eabf3978 (2021)
DOI: 10.1126/sciadv.abf3978

This PDF file includes:

Design of radiation shield

The function of the radiation shield is twofold: First, it reduces the unwanted contribution from atmospheric radiative heat gains $\dot{Q}_{\mathrm{atm}}$. In the sky transparency window, atmospheric radiation predominantly comes from large zenith angles (Θ), where the emissivity of the atmosphere is highest due to the increased pathlength of radiation through air (*45*). Thus, blocking thermal radiation of the atmosphere from large values of Θ enhances the cooling performance of the selective emitter. Second, the radiation shield aids direct thermal radiation from the selective emitter $\dot{Q}_{\mathrm{cool}}$ towards Θ = 0°, where the atmospheric transmittance is highest. Even thermal radiation emitted at large Θ is redirected towards Θ = 0°, because we design the radiation shield to be highly reflective in the 8-13 μm wavelength range. Therefore, the radiation shield maximizes $\dot{Q}_{\mathrm{dew}}$ (see equation (1) in the main text) and thus the dewing potential of the selective emitter. This can only be achieved if all of the most important heat transfer terms, i.e. incoming $\dot{Q}_{\mathrm{atm}}$ as well as outgoing thermal radiation $\dot{Q}_{\mathrm{cool}}$ are considered.

In order to reduce radiative heat gains from the atmosphere, we designed the shield in the shape of a truncated cone, where the emitter resides at its smaller base with radius r. The truncated cone is further parametrized by its half-opening angle β and height H, as shown in Fig. 2A of the main text. We fixed r = 7.4 cm, so that the shield does not come into contact the 4-inch sized emitter. Moreover, H is set to 25 cm to prevent wind gusts causing the shield to fall over. The radiation shield is fabricated from a 0.5 mm thick aluminum sheet and both its inner and outer surfaces are covered with reflective aluminized Mylar. The aluminum sheet is then shaped into a cone and mounted to the device, completely isolated from the emitter.

To determine the optimal angle *β,* we modeled the spatial and spectral dependence of the atmospheric emissivity $\varepsilon_{\mathrm{atm}}(\Theta,\lambda)$ according to a box model (*42*), assuming a constant atmospheric transmittance of 0.87 at Θ = 0° across the sky window and unity emissivity with Lambertian distribution outside this spectral range (*40*). We then project the hemispherical distribution of the sky onto a disk, which covers the top of the radiation shield, and randomized rays according to $\varepsilon_{\mathrm{atm}}(\Theta,\lambda)$. We account for the experimental constraints of *H* and *r*, and run simulations from $2° \leq \beta \leq 46°$ with 2° step size (higher angles are not considered due to the footprint of the system). We employed the geometrical raytracing module in COMSOL with 400,000 starting rays and for 3 different reflectivity values *R* of Mylar (*R* = 0.98, 0.95, 0.92). With these results, we obtain a reduction factor for atmospheric rays inside and outside the sky window impinging onto the selective emitter, for each *R* and *β*. We follow the same procedure for $\dot{Q}_{\mathrm{cool}}$, however this time rays start from a disk at the bottom of the radiation shield (i.e. where the selective emitter resides) with Lambertian distribution.

To quantify the impact of the radiation shield on the cooling power $\dot{Q}_{\mathrm{cool}}$ and the reduction of atmospheric heat gains $\dot{Q}_{\mathrm{atm}}$, we compute these heat fluxes. For a fair comparison, we fix the sample and ambient temperatures to 20 °C and compute $\dot{Q}_{\mathrm{cool}}(T_{\mathrm{sample}}) = \int \cos(\Theta) d\Omega \int_{0.2\ \mu\mathrm{m}}^{20\ \mu\mathrm{m}} I_{\mathrm{BB}}(T_{\mathrm{sample}},\lambda)\varepsilon_{\mathrm{sample}}(\lambda) d\lambda$, where λ is the wavelength, $I_{\mathrm{BB}}(T_{\mathrm{sample}},\lambda)$ the blackbody radiation intensity according to Planck's law, $\varepsilon_{\mathrm{sample}}(\lambda)$ the spectral emissivity of the selective emitter and $\int d\Omega$ represents the integral over all solid angles. For a given opening angle *β,* one can define a shielding angle φ (see Fig. 2A in the main text), which can be geometrically interrelated by $\tan\varphi = H/\left(2r + H\tan\beta\right)$. Atmospheric radiation originating from Θ

> (90°-*φ)* is now shielded and can not intercept the emitter. Thus, $\dot{Q}_{\mathrm{atm}}$ is expressed as $\dot{Q}_{\mathrm{atm}}(T_{\mathrm{amb}}) \approx 2\pi\int_{0}^{90°-\varphi}\int_{0.2\ \mu\mathrm{m}}^{20\ \mu\mathrm{m}} I_{\mathrm{BB}}(T_{\mathrm{amb}},\lambda)\varepsilon_{\mathrm{atm}}(\Theta,\lambda)\varepsilon_{\mathrm{sample}}(\lambda)d\lambda\cos\Theta\sin\Theta d\Theta$. Here, we consider the spectral and spatial dependence of the atmospheric emissivity $\varepsilon_{\mathrm{atm}}(\Theta,\lambda)$ and differentiate between atmospheric radiation coming from wavelengths inside and outside the atmospheric transparency window. The individual fluxes, as can be seen in the expression for $\dot{Q}_{\mathrm{atm}}$, are numerically integrated from 200 nm to 20 μm, since we obtained the spectral properties of the selective emitter in this range. Next, we weight each heat flux accordingly with the reduction factor received through the geometrical raytracing simulations.

As shown in Fig. S1, some non-negligible absorption of Mylar (i.e. $R < 1$) reduces the amount of $\dot{Q}_{\mathrm{cool}}$ that can leave the radiation shield and be dissipated in cold space, thus reducing the cooling power of the selective emitter. A smaller β means more reflection of the thermal emission $\dot{Q}_{\mathrm{cool}}$ with a larger fraction reabsorbed by the shield. In contrast, a smaller β shields the selective emitter more from atmospheric radiative heat gains and thus reduces $\dot{Q}_{\mathrm{atm}}$. Accounting for its absolute values, we find that the optimal range of β is $25° \leq \beta \leq 30°$ dependent on R, as indicated in Fig. S1. Aside of shielding the selective emitter from atmospheric radiation, in the morning and evening hours, when the sun zenith angle $\Theta > (90° - \varphi)$, the radiation shield blocks direct solar radiation. Moreover, the shielding of radiation from high Θ allows the system to operate even in the vicinity of buildings.

While we carried out this analysis based on the optical properties of our selective emitter, this strategy of properly shielding from environmental radiative heat gains can be applied for any selective emitter to enhance the dewing potential. Fig. S2 shows how the radiation shield reduces

$\dot{Q}_{\mathrm{atm}}$ within the 8–13 μm wavelength range. Hence, accounting for the spatial dependence of the atmospheric emissivity would also significantly enhance the performance of a perfectly selective emitter in the 8–13 μm wavelength range. Finally, we would like to stress that $\dot{Q}_{\mathrm{cool}}$ would be seriously impaired if the spatial selectivity were to be incorporated into the design of the selective emitter. Limiting the angular emissivity of the selective emitter would reduce the total emitted power $\dot{Q}_{\mathrm{cool}}$, as it would block a range of radiative channels and minimize the overall emitter emissivity. Consequently, one must account for the atmospheric heat gains through a dedicated device component, here our specifically designed radiation shield. This allows to maintain a high overall emissivity while shielding the selective emitter from the detrimental heat gains.

Procedure for subcooling experiments

We performed all outdoor experiments on the roof of a building at ETH Zurich (Latitude 47.377747, Longitude 8.547607). We placed a 4-inch diameter OPUR-foil sample and two selective emitter samples each on a 19 × 19 × 6 cm Styrofoam block and covered them with an insulating polyethylene film to minimize convective heat gains. We measured the sample temperature with T-type thermocouples (Omega HSRTC-TT-T-36-36) and a thermocouple logger (Lutron TM-947SD). Prior to the experiments, all thermocouples were calibrated (Fluke 9142). We recorded ambient temperature with a T-type thermocouple (Omega HSRTC-TT-T-36-36) connected to a small copper plate (2 × 1 × 0.5 cm) inside a weather station shield (TFA Dostmann). Two experiments demonstrate the beneficial effect of the radiation shield. During the experiment on May 16, 2019 (see Fig. S3), we recorded the subcooling performance of two samples for 1.5 hours. Then, we added the radiation shield to sample 1. For the experiment on May 23, 2019 (see Fig. S4), the radiation shield was first placed on sample 1, 2.5 hours after the start of the experiment. Then, we removed the shield from sample 1 and, 1.5 hours later, placed on sample 2. By doing this, we can exclude any effect of inherent fabrication differences of the optical properties of the emitters in the experiments. Both Fig. S3 and Fig. S4 evidence that, although in both cases one of the samples shows an initially slightly different cooling performance, this effect is clearly overtaken by the radiation shield. A further 24-hour experiment on August 13/14, 2019, see Fig. S5, evidences the beneficial effect of the radiation shield even at night. As the atmospheric temperature is lower at night and solar radiation is not present, this effect is less dominant than during the day.

Quantification of heat fluxes

To determine how the radiation shield affects the individual instantaneous heat flux gains of the selective emitter, we quantify convective heat flux gains from the atmosphere $\dot{Q}_{\text{conv}}$. Further, we numerically integrate solar $\dot{Q}_{\text{sun}}$ and atmospheric radiative $\dot{Q}_{\text{atm}}$ heat gains from 200 nm to 20 µm. As outlined and indicated in Fig. 2A in the main text, we neglect heat gains from condensation ($\dot{Q}_{\text{dew}}$) at this point (results in Fig. S6), as the sample resides on an insulating Styrofoam block, preventing any condensation.

The convective heat flux is $\dot{Q}_{\text{conv}} = h_c(T_{\text{amb}} - T_{\text{sample}})$, where h_{c} is the convective heat coefficient, T_{amb} and T_{sample} ambient and the temperature of the emitter, respectively. We set h_{c} = 10 W m^{-2} K^{-1} and used experimental data for T_{amb} and T_{sample}.

To determine $\dot{Q}_{\text{sun}}$, we describe the solar heat flux absorbed by the selective emitter as $\dot{Q}_{\text{sun}} = \int_{0.2\ \mu\text{m}}^{20\ \mu\text{m}} \varepsilon_{\text{sample}}(\lambda)\Psi I_{\text{AM1.5}}(\lambda,\Theta)d\lambda$, where λ is the wavelength, $\varepsilon_{\text{sample}}(\lambda)$ the spectral emissivity of the selective emitter, Ψ a scaling factor adjusted to the experimentally measured solar irradiance, $I_{\text{AM1.5}}(\lambda,\Theta)$ the AM1.5 reference spectrum (ASTM G173-03 from SMARTS v. 2.9.2) and Θ the solar zenith angle (see Fig. 2A in the main text). We calculated Ψ by accessing Global Horizontal Irradiance data (MeteoSwiss, station "Fluntern", pyranometer from Kipp&Zonen, CM21) and dividing it by the integral of the AM1.5 reference spectrum. We accessed solar zenith angle data for the coordinates of the experiment location (Latitude 47.377747, Longitude 8.547607) from SolarTopo and set $\dot{Q}_{\text{sun}} = 0$ W m^{-2} whenever the sun zenith angle $\Theta > (90° - \varphi)$, where φ is the shielding angle of the radiation shield (see Fig. 2A in the main text). $\varepsilon_{\text{sample}}(\lambda)$ is measured with a UV/VIS NIR spectrometer (V770) with a ILN-925 integrating sphere at normal incidence. We determine infrared properties with a FTIR spectrometer (Thermo Fisher Scientific) along with a gold-coated IR integrating sphere (Pike technologies).

We approximated the atmospheric radiative heat flux intercepted by the selective as $\dot{Q}_{\mathrm{atm}}(T_{\mathrm{amb}}) \approx 2\pi \int_{0}^{90°-\varphi} \int_{0.2\ \mu\mathrm{m}}^{20\ \mu\mathrm{m}} I_{\mathrm{BB}}(T_{\mathrm{amb}}, \lambda) \varepsilon_{\mathrm{atm}}(\lambda, \Theta) \varepsilon_{\mathrm{sample}}(\lambda) d\lambda \cos\Theta \sin\Theta d\Theta$, where the atmospheric emissivity $\varepsilon_{\mathrm{atm}}(\lambda, \Theta)$ is calculated according to a box model (*42*) and for the emissivity at $\Theta = 0°$, we used ModTran5 data from previous literature (*34*). To compute $I_{\mathrm{BB}}(T_{\mathrm{amb}}, \lambda)$, we use experimental ambient temperature and Planck's law. Moreover, for simplification, the interior walls (Mylar) of the radiation shield are assumed to be perfectly reflective.

As indicated in Fig. S6, the radiation shield (bottom graph) strongly reduces heat gains from the atmosphere ($\dot{Q}_{\mathrm{atm}}$), manifested in a higher subcooling of the selective emitter. The higher temperature gradient leads to an increase in convective heat gains $\dot{Q}_{\mathrm{conv}}$ from ambient.

Procedure for dew harvesting experiments

We performed dew harvesting experiments on the roof of an ETH Zurich building (Latitude 47.377747, Longitude 8.547607). The experimental chamber (outer dimensions 45 × 45 × 28 cm) is made out of 1 cm thick PMMA and its outer surface is coated with aluminized Mylar (Oxford Instruments) to prevent heating. We installed the chamber on an extruded polystyrene plate to reduce vibrational noise and conductive heating from the roof when hot. The selective emitter sits on a 1 cm-thick Styrofoam ring supported by a PMMA structure, which itself is connected to a load-cell type precision scale (G&G, JJ200B) with a resolution of 0.001 g (see Fig. S7). We tested the long-term stability of the scale with an experimental run at 80-85% relative humidity, where we did not place a selective emitter onto the Styrofoam ring. An insulating polyethylene film prevents convection and is spanned 2 cm above the selective emitter. We recorded the temperature inside the chamber with a T-type thermocouple (Omega HSRTC-TT-T-36-36) and a thermocouple logger (Lutron TM-947SD). Due to the low thermal mass of the chamber, the air temperature inside is convectively equilibrated (due to wind) with the ambient temperature. Hence, the air temperature inside the chamber is very close to the ambient temperature (see Fig. S8). We record relative humidity and the temperature inside the chamber with a Sensirion SHT31 Smart Gadget Development Kit. Air is mixed by a fan (FORCECON DFB803812MDOT) inside the chamber to achieve rapid and homogeneous diffusion of water vapor inside the chamber, and we turned off the fan before the start of the experiments (to ensure fully passive operation). To reach the desired relative humidity, we designed two petri dish stacks filled with supersaturated salt solutions (see Fig. S7 where, for illustration purposes, we removed one of the stacks). We ran experiments at 95% (millipore H_2O), 90% (K_2SO_4), 80-85% (KCl) 75% (NaCl) and 65% ($MgCl_2$ and K_2SO_4) relative humidity. We recorded ambient temperature T_{amb} with a T-type thermocouple (Omega

HSRTC-TT-T-36-36) attached to a small copper plate (2 × 1 × 0.5 cm) inside a weather station shield (TFA Dostmann). Before the start of each experiment, we synchronized all timestamps. Global Horizontal Irradiance is retrieved from MeteoSwiss (station "Fluntern", pyranometer from Kipp&Zonen, CM21). Table S1 sums up all results.

Proof-of-concept outdoor experiments

We performed two qualitative outdoor experiments to demonstrate the concept of our atmospheric water harvesting system. In the first experiment from October 8, 2020, 10:00 until October 10, 2020, 01:00, we placed a selective emitter with the CNF coating on its bottom side on our experimental chamber. Therefore, the CNF coating was exposed to humid air (RH ≈ 90-95%) using a supersaturated K_2SO_4 salt solution inside the chamber (see Fig. S12A). However, unlike in previous experiments, we removed the scale and replaced it with a jack. We placed the chamber at the same location where we had carried out previous outdoor experiments (rooftop of a building at ETH Zurich, Switzerland). Instead of measuring the instantaneous mass, we placed a petri dish underneath the CNF coated selective emitter to collect the self-removed condensate after 39 hours, as shown in Fig. S12B.

For the second experiment (October 14, 2020, 17:00 until October 15, 2020, 11:00), we mounted a selective emitter with radiation shield onto a Styrofoam box, which had a cut-through opening in it. As schematically illustrated in Fig. S12C, the bottom side (CNF coating) was thus exposed to ambient air with fluctuating relative humidity (mean RH: 83%). Underneath the collection surface, a petri dish served as a collection reservoir for the passively removed water. Fig S12D demonstrates that our system is capable of harvesting atmospheric water under real-world conditions—through the night and into the day—in a completely passive manner.

Supplemental figures

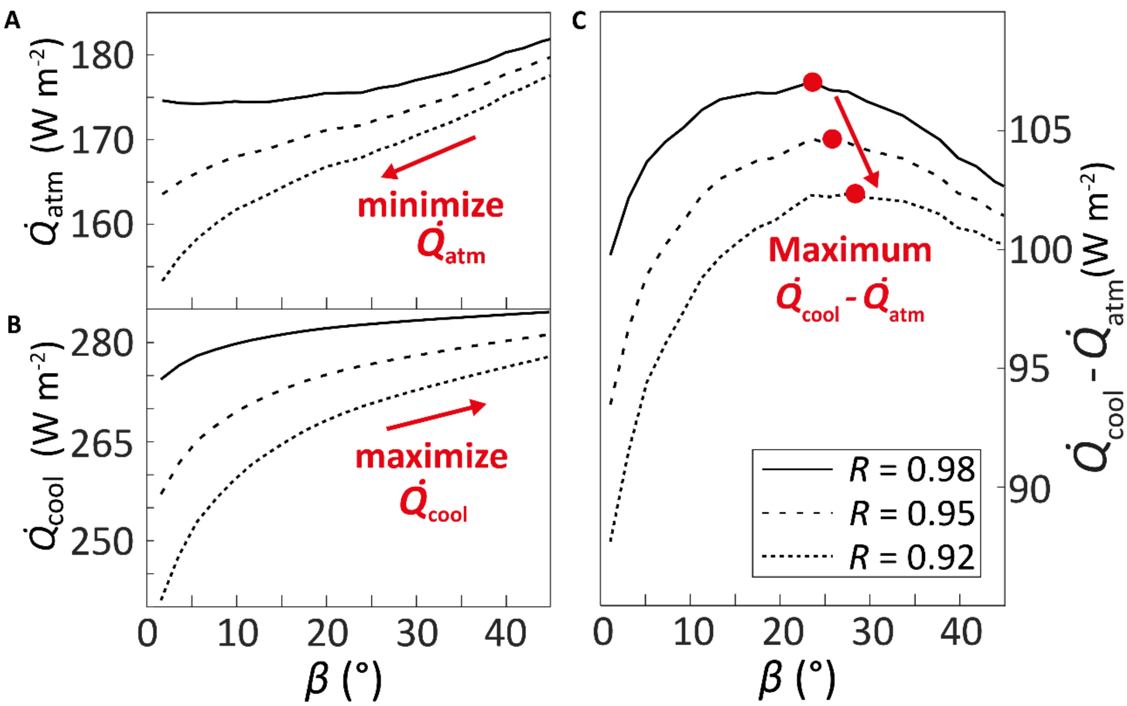

Fig. S1. Raytracing simulation to determine optimum half-opening angle of the radiation shield. (A) To maximize $\dot{Q}_{dew}$ in equation (1) of the main text, the radiation shield maximizes $\dot{Q}_{cool}$ while reducing $\dot{Q}_{atm}$. Here, we neglect solar $\dot{Q}_{sun}$ and convective $\dot{Q}_{conv}$ heat gains. The results of a geometrical raytracing simulation (400,000 starting rays) with fixed radiation shield smaller base radius r = 7.4 cm and height H = 25 cm are shown. Intercepted radiative heat gains from the atmosphere $\dot{Q}_{atm}$ get reduced by lowering the half-opening angle β of the radiation shield. **(B)** A smaller β has the beneficial effect of reducing $\dot{Q}_{atm}$, however less cooling power of the emitter $\dot{Q}_{cool}$ exits the radiation shield. This reduction effect becomes even more dominant when the Mylar reflectivity R decreases, as $\dot{Q}_{cool}$ is absorbed by the interior of the radiation shield walls. **(C)** The combined interplay of these results leads to an optimum $\beta \approx 30°$ (non-perfect reflectivity of Mylar $R \approx 0.92$–0.95). Values for $\beta > 46°$ are not considered due to the footprint of the system.

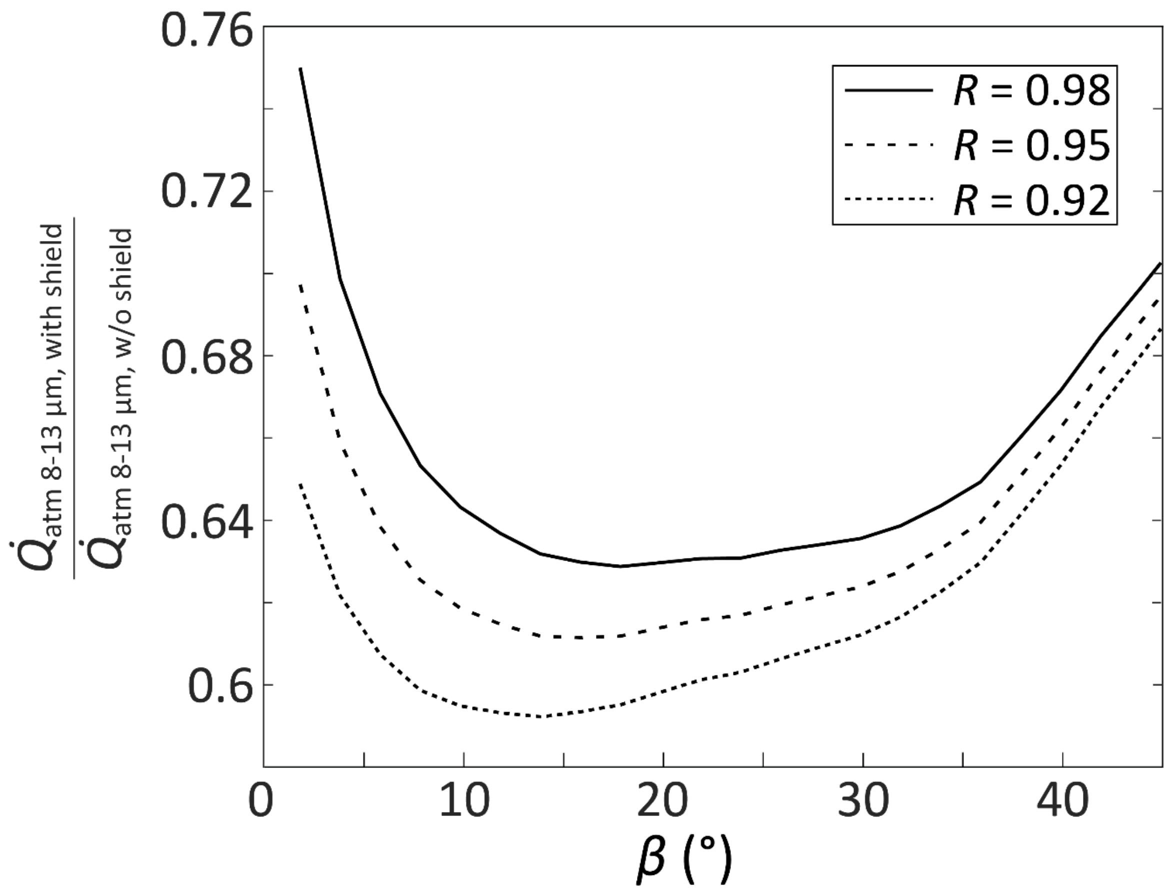

Fig S2. Radiation shield reduces atmospheric heat gains within the sky transparency window. Geometrical raytracing results show how the incident atmospheric heat gains of the emitter within the 8–13 µm range are significantly reduced. For our radiation shield (half-opening angle $\beta\approx30°$), atmospheric heat gains are reduced by ~36–39%. Shown are the results for 3 different reflectivity values of Mylar *R*.

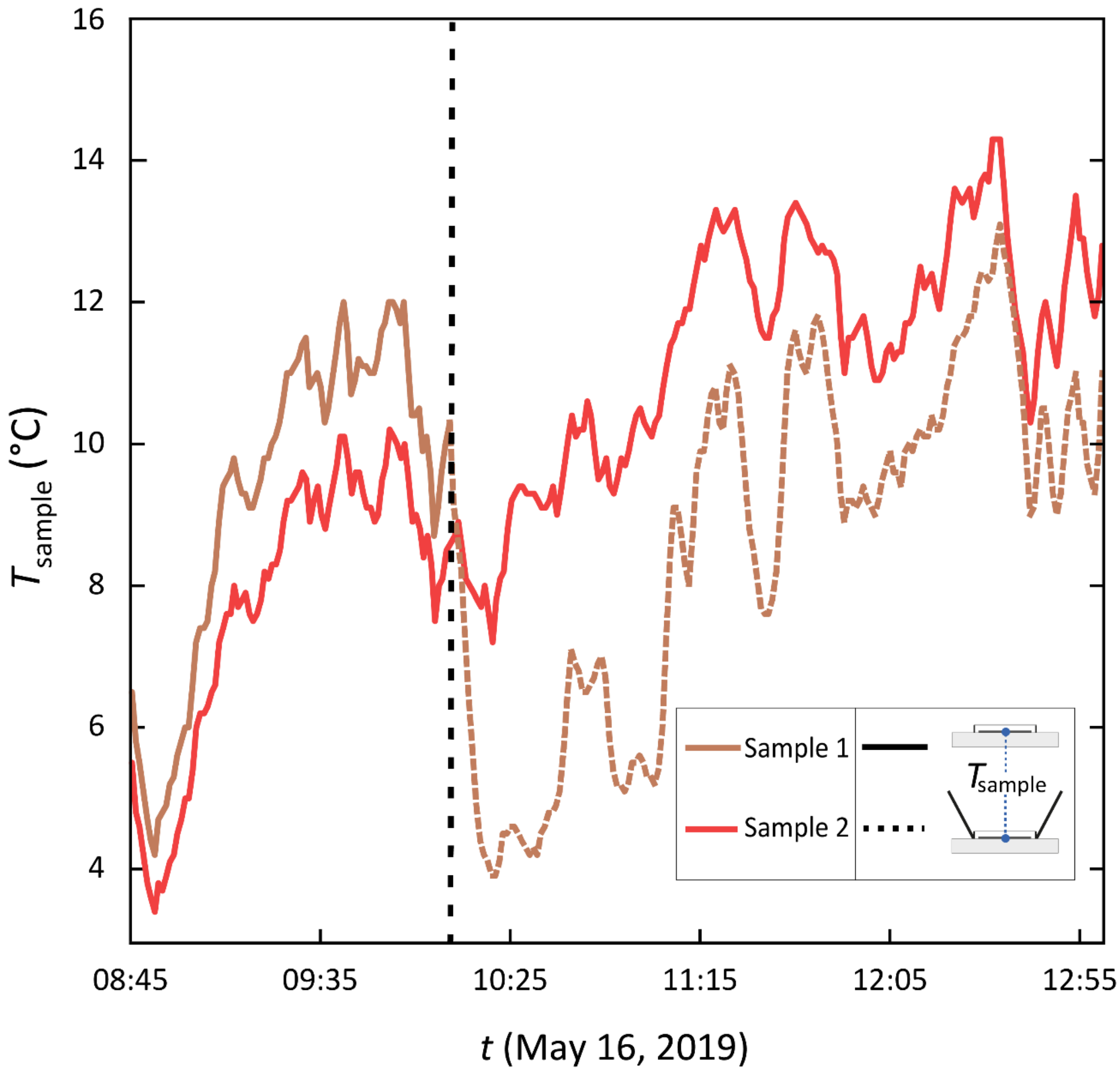

Fig. S3. Demonstration of subcooling enhancement through radiation shield. We tested the subcooling performance of two identical selective emitter samples, resting on a Styrofoam box by measuring their temperature T_{sample}. At 10:10, the radiation shield was placed on sample 1 (brown line), leading to an immediate enhanced subcooling (lower sample temperature T_{sample}) compared to sample 2 (red line).

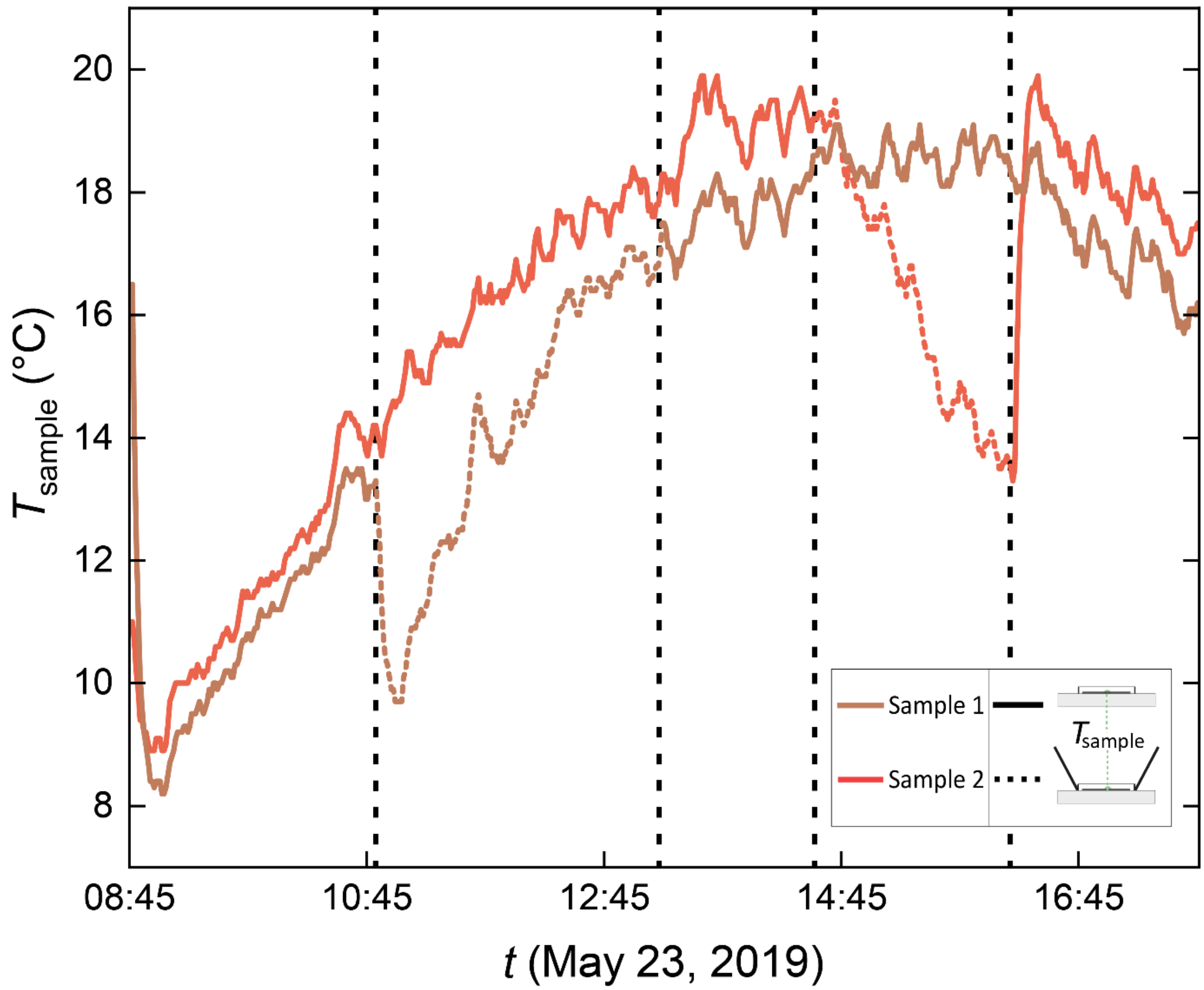

Fig. S4. Effect of radiation shield independent of the selective emitter. We tested the subcooling performance of two identical selective emitter samples, resting on a Styrofoam box by measuring their temperature T_{sample} .To verify that the effect of the radiation shield is independent of the selective emitter, we switched the radiation shield between sample 1 (brown line) and sample 2 (red line). It is unmistakably visible that the effect of the radiation shield does not depend on the sample. This implies that—if a proper half-opening angle of the shield is determined—the radiation shield can be used synergistically with any selective emitter.

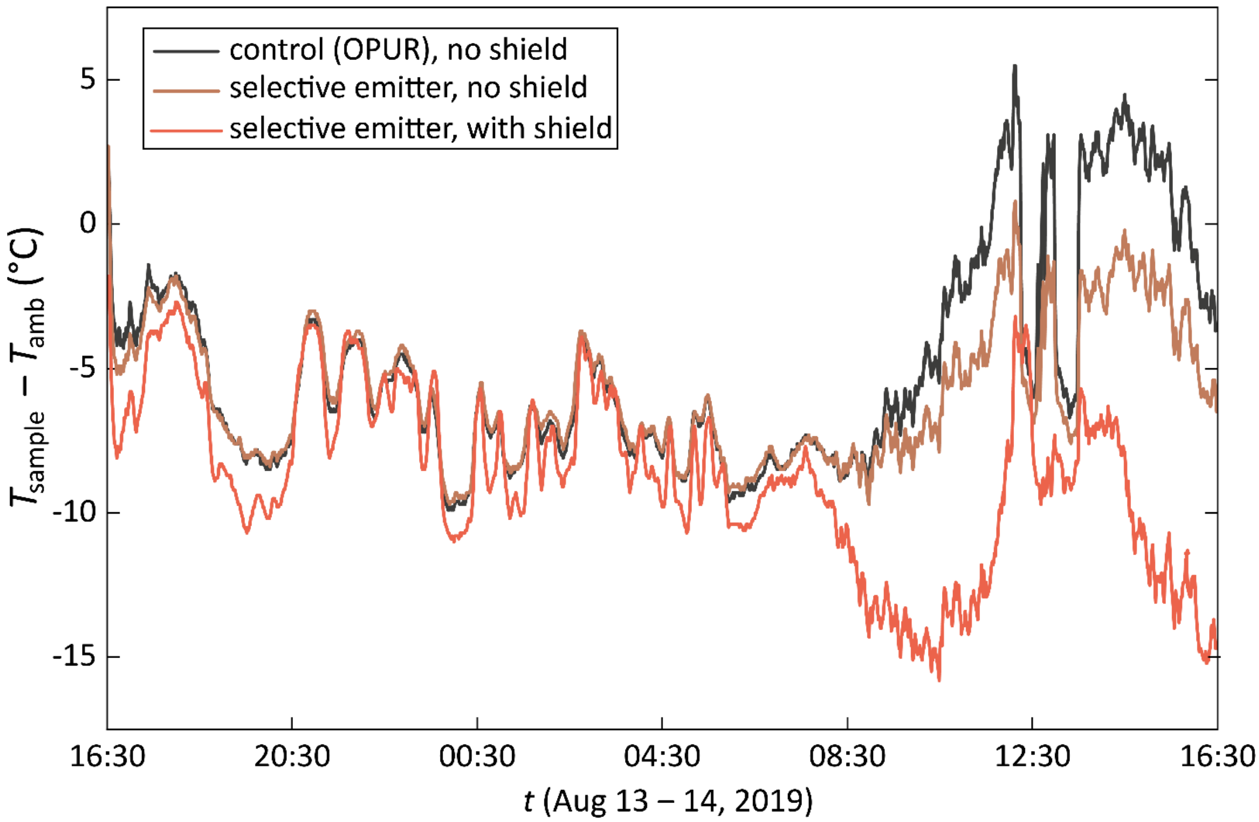

Fig. S5. 24-hour continuous subcooling enhancement through the radiation shield. The beneficial effect of the radiation shield is also observable at night during a 24-hour experiment on August 13/14, 2019. As the atmospheric temperature is lower at night and solar radiation is not present, this effect is less dominant than during the day. The three distinct peaks around 12:30 and 13:00 and 14:00 arise due to cloud formation, reducing the sky transparency and deteriorating the cooling ability.

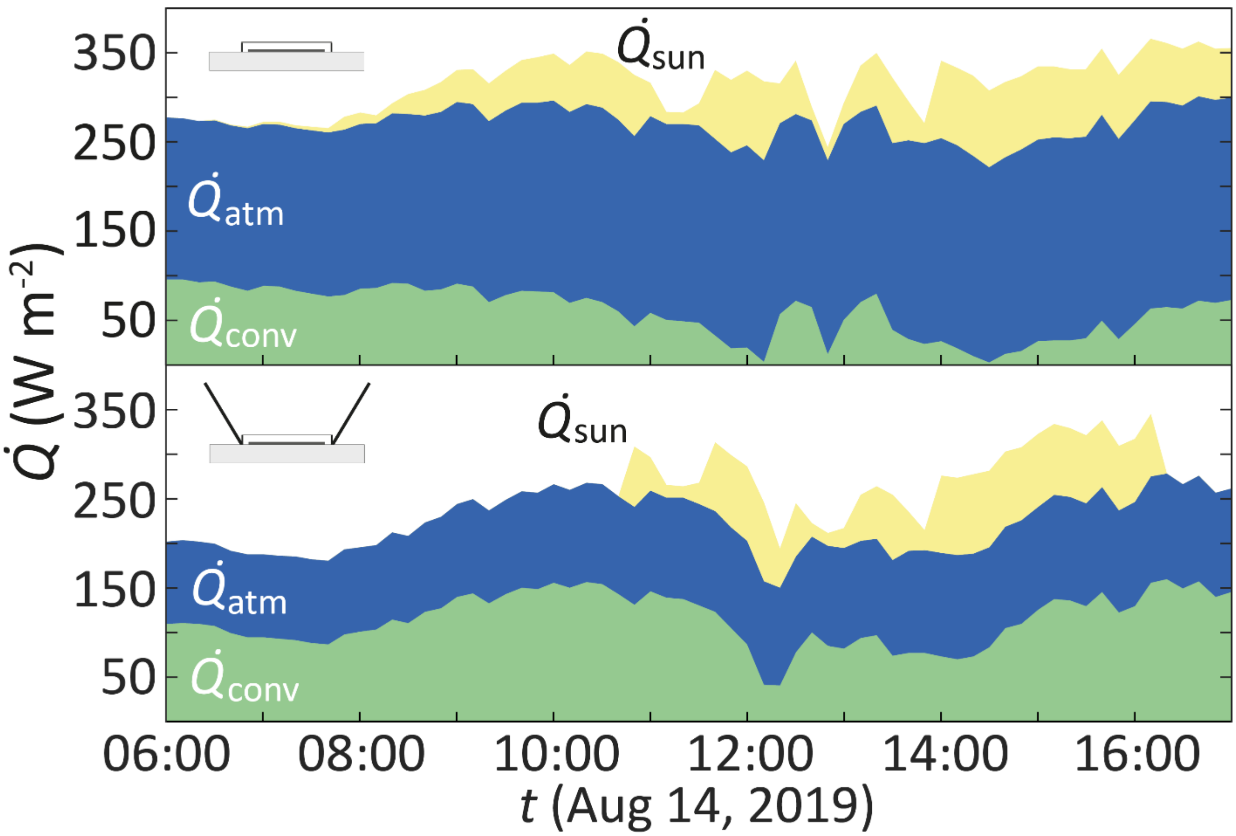

Fig. S6. Heat flux comparison of selective emitter without (top) and with (bottom) radiation shield. We quantified the effect of the radiation shield during the experiment on August 14, 2019, by calculating the according heat terms (based on experimental solar radiation, temperature of ambient and the selective emitter). The radiation shield accounts for the complete radiative environment and considerably reduces atmospheric heat gains $\dot{Q}_{atm}$. Due to this heat gain reduction, the selective emitter with radiation shield (bottom) reaches a lower temperature, which in turn leads to an increase in convective heat gains $\dot{Q}_{conv}$.

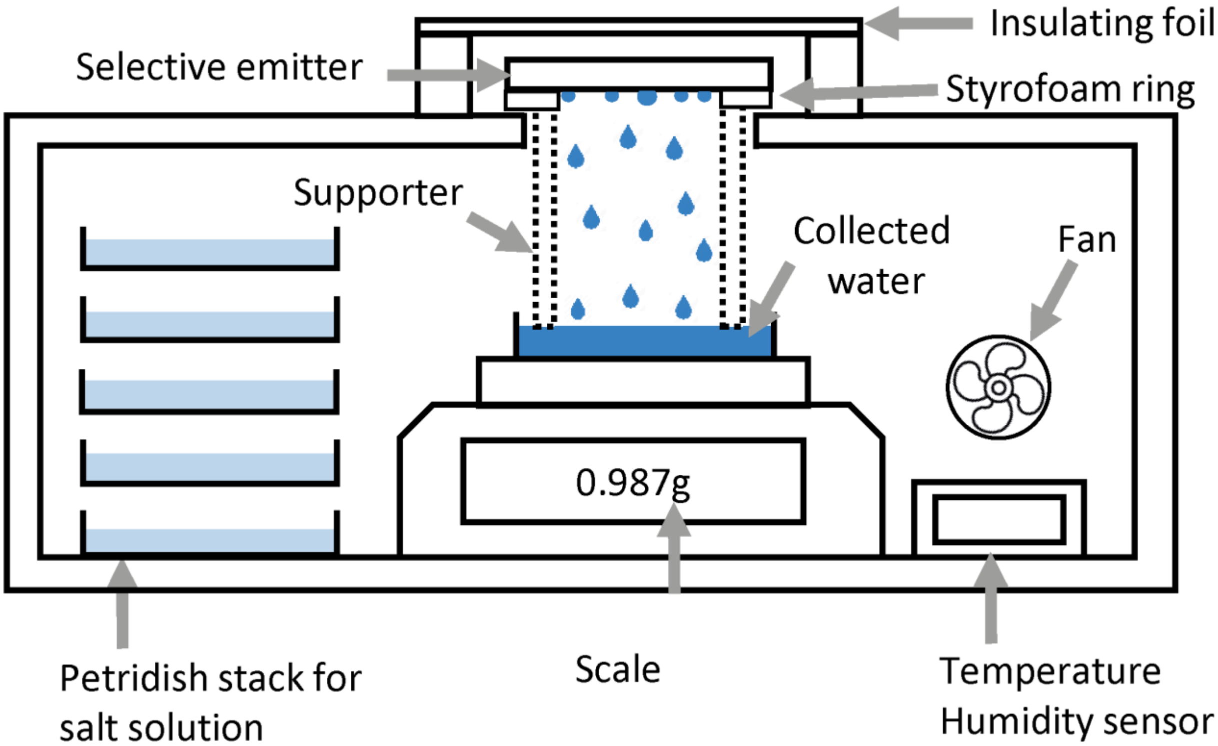

Fig. S7. Schematic of the interior of the outdoor experimental chamber. For outdoor dew harvesting experiments, we built an experimental chamber to create a constant relative humidity environment by using supersaturated salt solutions in a petri dish stack. The condensed dew is measured with a load-cell type scale. Additionally, a custom-built, freestanding PMMA structure with a Styrofoam ring holds the selective emitter. The insulating foil on top protects the selective emitter from convective heat gains.

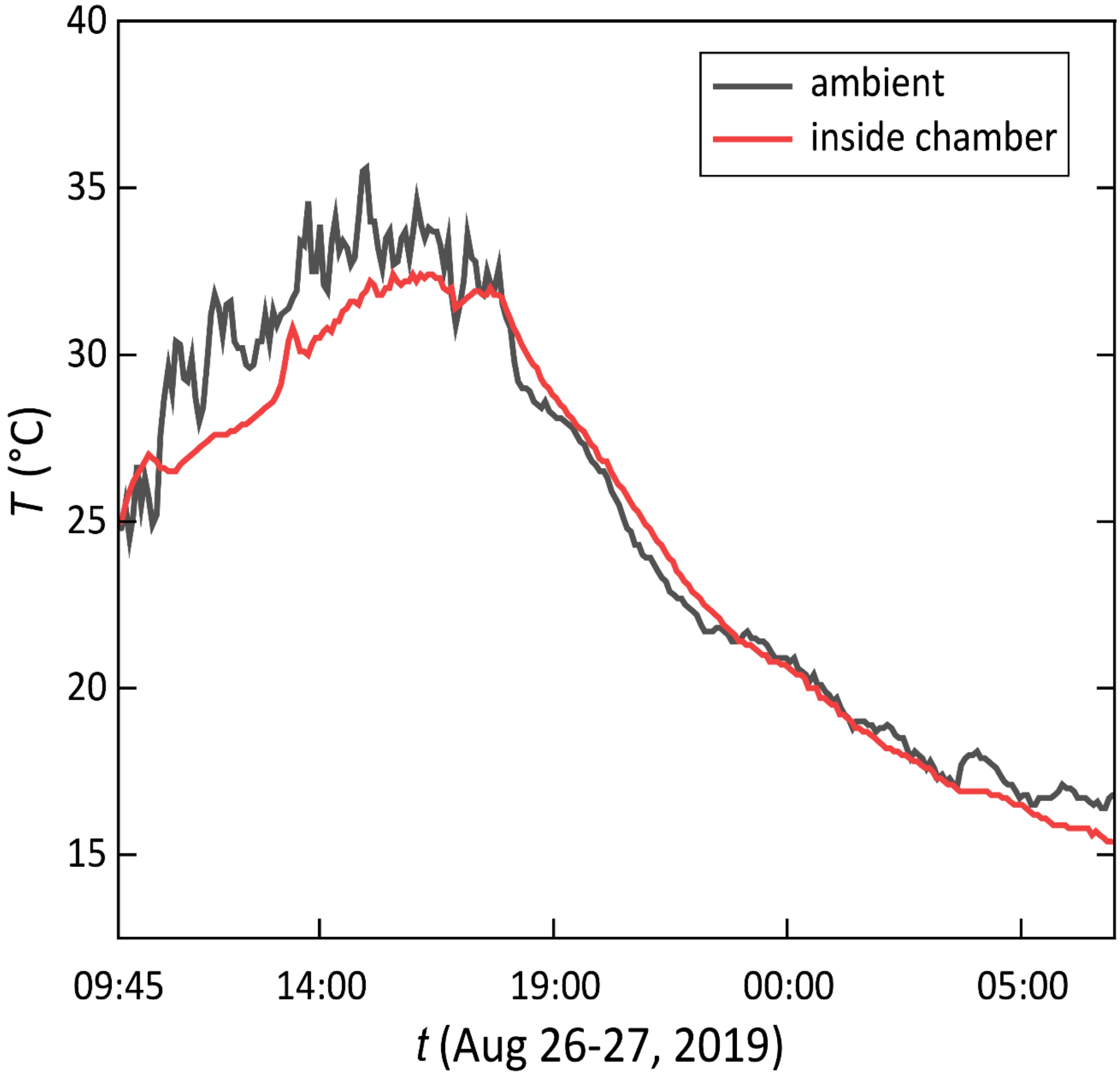

Fig. S8. Passive temperature control in the experimental chamber through natural convection. Data taken from 24-hour experiment on August 26/27, 2019. The temperature inside the experimental chamber closely follows ambient temperature (both measured with a T-type thermocouple attached to a small copper plate), as the chamber volume is kept to a minimum (low thermal mass). Reflective Mylar on the outside walls of the experimental chamber prevents it from solar heating (greenhouse effect).

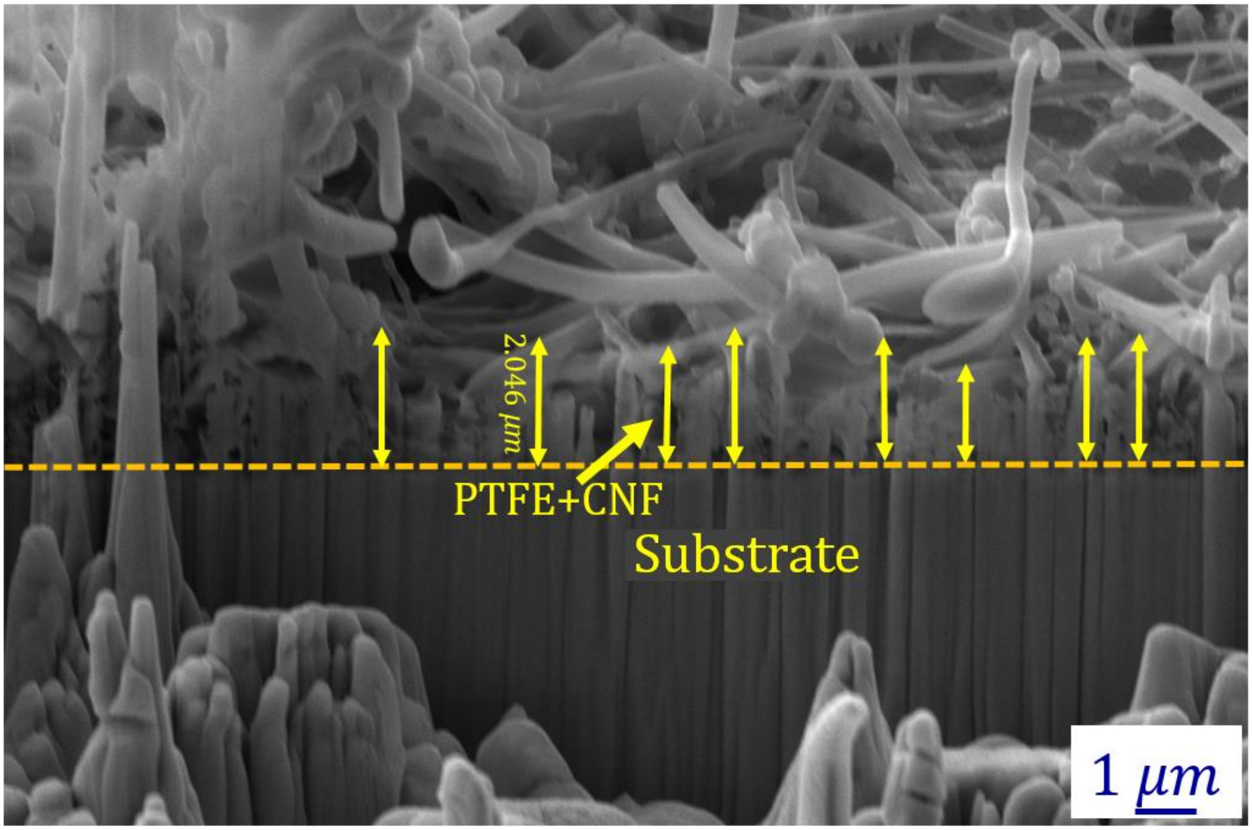

Fig. S9. Thickness measurement of the CNF coating with FIB. The sample was cut with focused ion beam milling (FIB) to reveal the thickness of the superhydrophobic coating, which was determined to be ~2 µm.

A

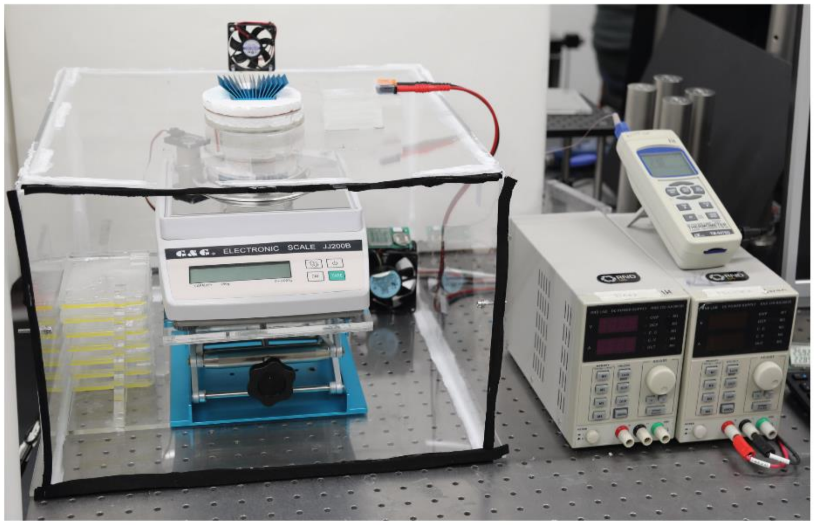

B

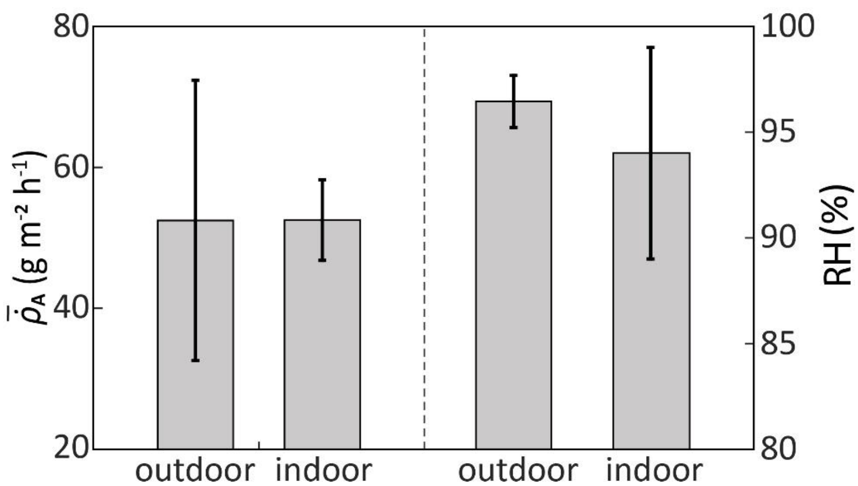

Fig S10. Indoor dew harvesting setup. (A) For the indoor experiments, we rebuilt the outdoor experimental chamber. Supersaturated salt solutions are used to maintain a constant relative humidity (RH), a load-cell type scale measures the dew mass flux. The cooling power of the sample is controlled with a fan-cooled Peltier element. **(B)** To be comparable with outdoor experiments, we adjusted the cooling power such that $\bar{\dot{\rho}}_A$ (left panel) and RH (right panel) resemble the conditions during the outdoor experiment on August 30, 2019.

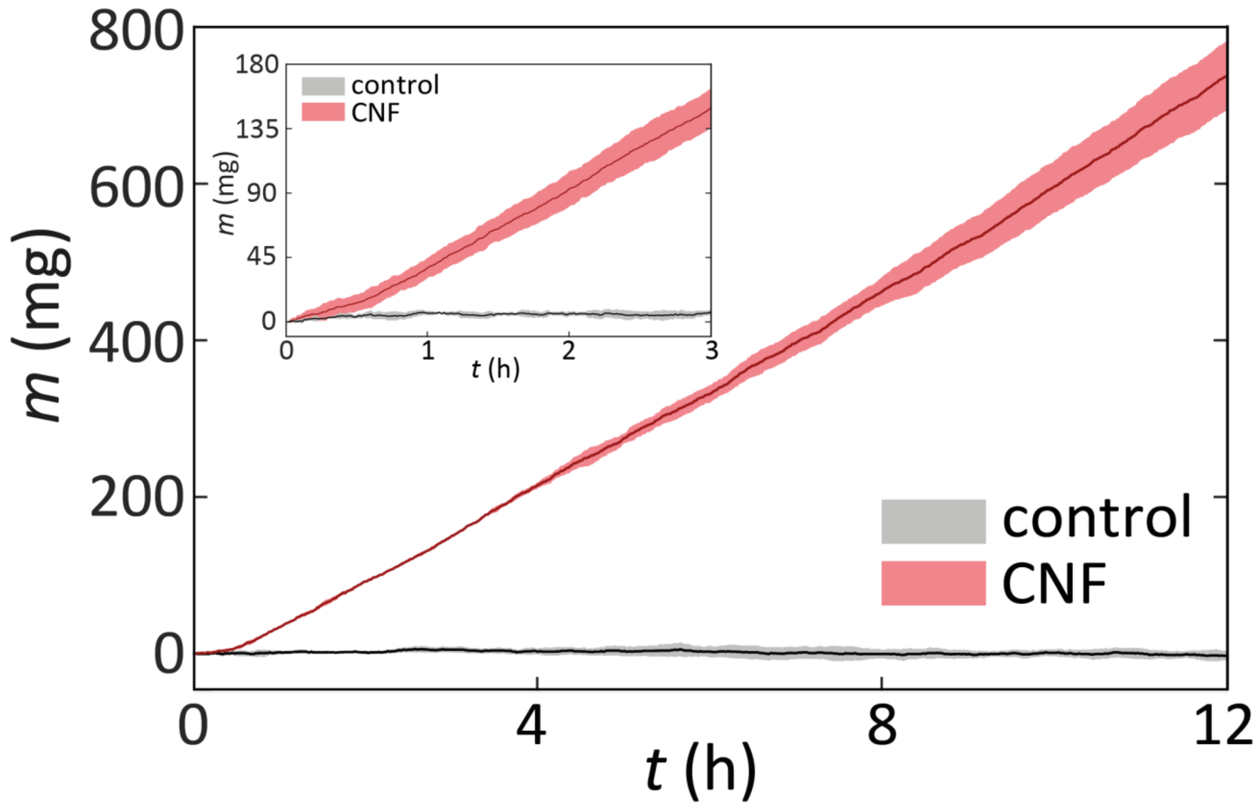

Fig S11. Comparison of passively collected water beneath the condenser with carbon nanofiber (CNF) superhydrophobic coating and without superhydrophobic coating (control). Both 3-hour (inset) as well as 12-hour experiments (N = 3 each) show the necessity of the superhydrophobic coating for complete passiveness of the atmospheric water harvesting system, as no water detaches from the control surface (RH > 90%).

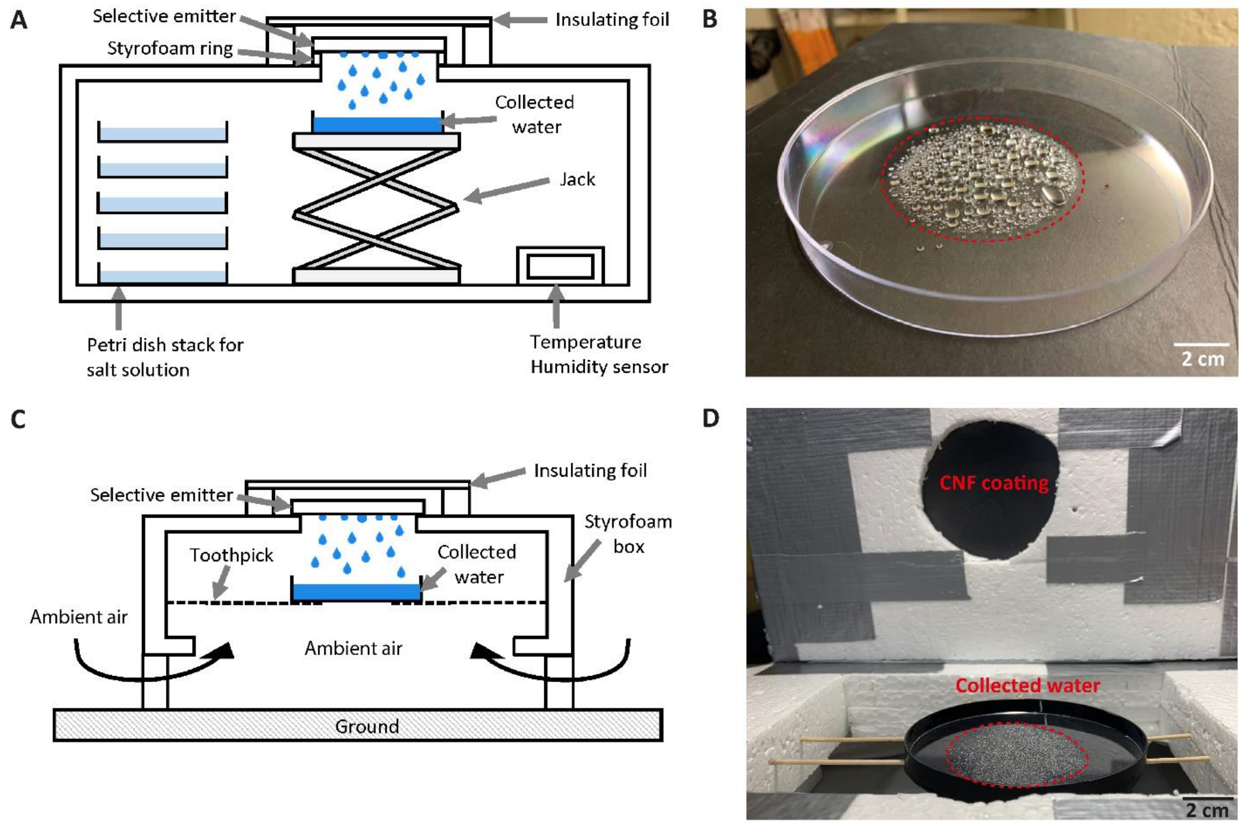

Fig. S12. Proof-of-concept outdoor experiments with CNF coating. (A) For the first proof-of-concept experiment, the previous experimental chamber (see Fig. S7) is used. However, the scale is removed and replaced with a jack. **(B)** Compeletely passive, self-removed and collected water during the first experiment from October 08, 2020, 10:00 until October 10, 2020, 01:00. The relative humidity inside the experimental chamber was set to ~90-95%. **(C)** For the second experiment, the selective emitter resided on a Styrofoam box with a cut-through hole to expose the condenser side to ambient air. A petri dish rests underneath the selective emitter, held by toothpicks. Ambient humid air can flow to the condenser side through the bottom of the Styrofoam box. **(D)** Collected water during the second experimental run (October 14, 2020, 17:00 until October 15, 2020, 11:00) at a mean ambient relative humidity of 83%. All experiments were carried out on the rooftop of a building at ETH Zurich, Switzerland.

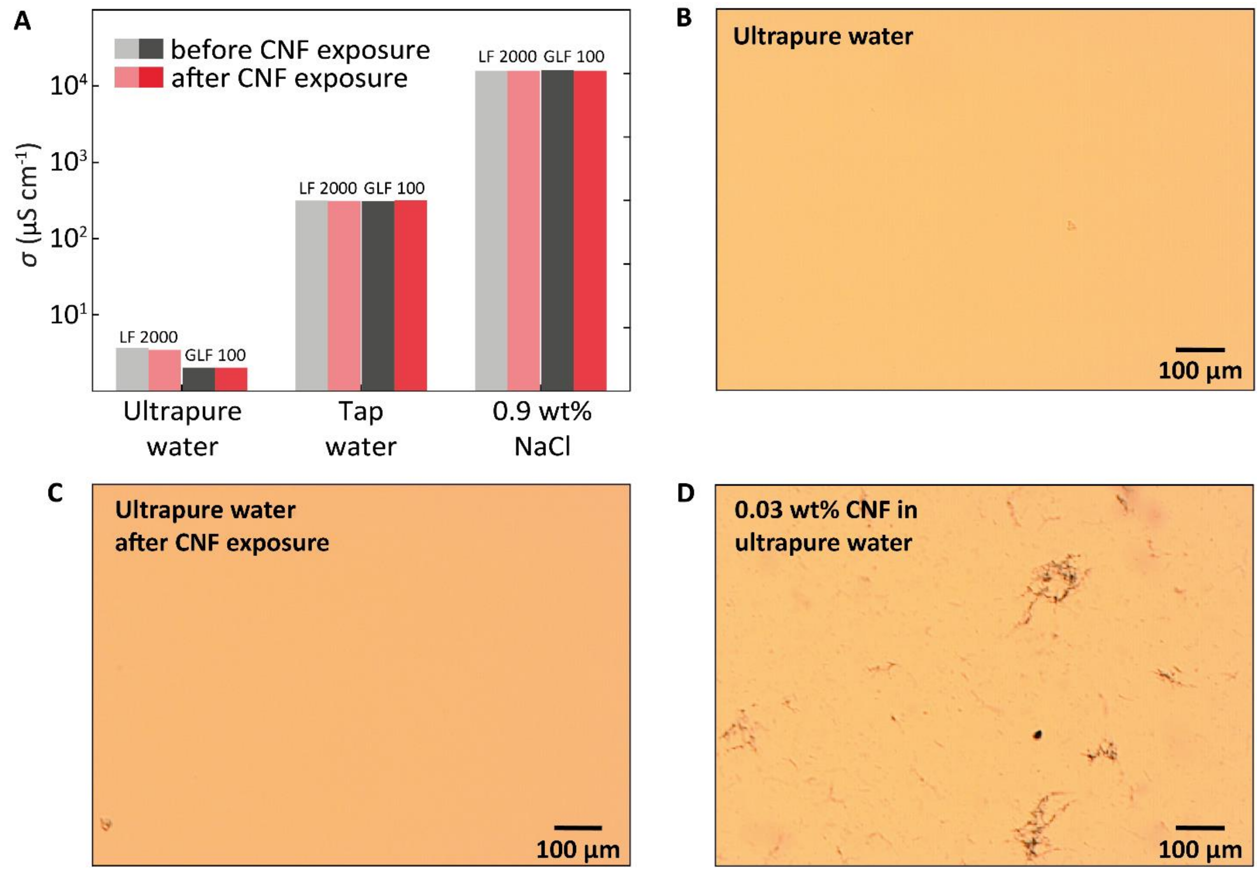

Fig S13. Water quality analysis demonstrates no detachment of CNF or CR ions traces. (A) The conductivity σ of water solutions (measured with 2 different tools) does not change upon exposure to the CNF coating, indicating no detachment of Cr ions. Bright field microscopy images of **(B)** ultrapure water, **(C)** ultrapure water after CNF exposure and **(D)** for comparison a 0.03 wt% CNF dispersion in ultrapure water under identical observation conditions demonstrates that no CNF is traceable in the harvested water.

Supplemental Tables

Table S1. Broad operational capability under various levels of solar irradiation.

Date (2019)	t_{start}	$\Delta t = t_{\text{end}} - t_{\text{start}}$	$\bar{I} = \frac{1}{\Delta t}\int I dt$	$\bar{\dot{\rho}}_A = \frac{1}{\Delta t}\int \dot{\rho}_A dt$
Jul 30	10:30	08:25 h	737 W m^{-2}	11.8 g m^{-2} h^{-1}
Aug 26 / 27	09:44	24:00 h	273 W m^{-2}	19.3 g m^{-2} h^{-1}
Aug 30	17:25	02:43 h	199 W m^{-2}	52.5 g m^{-2} h^{-1}
Sep 3	15:15	04:15 h	415 W m^{-2}	40.3 g m^{-2} h^{-1}
Sep 12	10:12	09:25 h	524 W m^{-2}	24.8 g m^{-2} h^{-1}